Research
A SCIENCE PARTNER JOURNAL

RESEARCH ARTICLE

Single-Ion Anisotropy-Stabilized Short-Period Helimagnetism in Frustrated Chiral Co_5TeO_8

Priya R. Baral[1,2,3*], Ravi Yadav[3], Victor Ukleev[2,4], Thomas LaGrange[3], Ivica Živković[3], Wen H. Bi[3], Marek Bartkowiak[2], Robert Cubitt[5], Nina-Juliane Steinke[5], Vladimir Pomjakushin[2], Yurii Skourski[6], Henrik M. Rønnow[3], Oleg V. Yazyev[3], Arnaud Magrez[3], and Jonathan S. White[2*]

[1]Department of Applied Physics and Quantum-Phase Electronics Center, The University of Tokyo, Tokyo 113-8656, Japan. [2]PSI Center for Neutron and Muon Sciences, 5232 Villigen PSI, Switzerland. [3]Institute of Physics, École Polytechnique Fédérale de Lausanne (EPFL), CH-1015 Lausanne, Switzerland. [4]Helmholtz-Zentrum Berlin für Materialien und Energie, D-12489 Berlin, Germany. [5]Institut Laue–Langevin, Grenoble 38000, France. [6]Dresden High Magnetic Field Laboratory (HLD-EMFL), 01328 Dresden, Germany.

*Address correspondence to: priya.baral@epfl.ch (P.R.B.); jonathan.white@psi.ch (J.S.W.)

Citation: Baral PR, Yadav R, Ukleev V, LaGrange T, Živković I, Bi WH, Bartkowiak M, Cubitt R, Steinke N-J, Pomjakushin V, et al. Single-Ion Anisotropy-Stabilized Short-Period Helimagnetism in Frustrated Chiral Co_5TeO_8. *Research* 2026;9:Article 1334. https://doi.org/10.34133/research.1334

Submitted 14 November 2025
Revised 29 May 2026
Accepted 30 May 2026
Published 25 June 2026

Copyright © 2026 Priya R. Baral et al. Exclusive licensee Science and Technology Review Publishing House. No claim to original U.S. Government Works. Distributed under a Creative Commons Attribution License (CC BY 4.0).

Chiral spin textures in magnetic insulators promise magneto-electric (ME) spintronics with orders-of-magnitude lower power consumption than metallic systems. However, realizing the short magnetic periods required for high-density device integration remains difficult, as conventional Dzyaloshinskii–Moriya interaction (DMI)-based mechanisms typically constrain spiral periods to tens of nanometers. While theory predicts that strong single-ion anisotropy (SIA) on frustrated lattices can stabilize complex non-coplanar textures, the potential for using this mechanism to engineer such compact textures remains largely unexplored. Here, we report that a cubic chiral insulator Co_5TeO_8 provides an experimental example of this paradigm. Comprehensive neutron scattering and magnetometry reveal helimagnetic spirals with continuously tunable pitch of 5.7 to 10 nm embedded in a complex phase diagram spanning 8 distinct phases. Capacitance anomalies throughout the phase diagram indicate ME coupling, pointing to the possibility of future *E*-field control of these textures. The temperature and field dependence of the helical wavevector strongly support a scenario in which site-dependent SIA provides the leading contribution to the selection of the helical period from a frustration-induced degenerate manifold. Consistent with this interpretation, ab initio calculations place SIA approximately an order of magnitude above DMI, distinct from conventional helimagnets. Co_5TeO_8 thus offers an experimental realization of sub-10-nm helimagnetism and motivates a design principle for anisotropy-engineered correlated insulators.

Introduction

Non-coplanar magnetic states—ranging from topological skyrmions to chiral vortex lattices—are central to modern spintronics owing to their emergent electrodynamics and robust stability against weak perturbations [1–4]. Yet, these intricate multi-$\boldsymbol{Q}$ architectures typically nucleate from a more fundamental parent phase: the single-$\boldsymbol{Q}$ spiral state [5,6]. As the elementary building block of non-coplanar magnetic states, the single-$\boldsymbol{Q}$ spiral emerges when competing interactions preclude collinear spin alignment [7,8], making a microscopic understanding of its stability essential for engineering complex topological phases [9,10]. Conventionally, this stability is attributed to specific exchange pathways governed by crystal symmetry and electronic structure of the material: the anti-symmetric Dzyaloshinskii–Moriya interaction (DMI) in chiral noncentrosymmetric hosts [11–13], geometric frustration [14,15] or Fermi-surface-nested Ruderman–Kittel–Kasuya–Yosida (RKKY) interactions in centrosymmetric systems [16,17], and, in itinerant magnets, higher-order terms such as the biquadratic exchange interaction [18,19]. Crucially, while these diverse mechanisms successfully predict a wide array of noncollinear magnetic phases, they share a common paradigm in which spatial modulation is driven primarily by intersite exchange, with local energy scales typically treated as subleading.

Conversely, magnetic anisotropy—traditionally treated as a weak perturbative correction—can fundamentally restructure the magnetic energy landscape when its magnitude rivals the exchange energy scales [20–22]. In isotropic Heisenberg models, single-$\boldsymbol{Q}$ helices are generically favored as a simple harmonic modulation preserves the fixed-moment constraint, whereas multi-$\boldsymbol{Q}$ superpositions tend to generate amplitude modulations that require higher harmonics to restore normalization. However, this exchange cost can be offset by strong easy-axis single-ion anisotropy (SIA), which, aided by thermal softening of the longitudinal spin stiffness [20], promotes multi-$\boldsymbol{Q}$ formation. On frustrated lattices, this mechanism stabilizes

a hierarchy of exotic phases, including the skyrmion lattice [23]. Moreover, in multi-sublattice magnets, inequivalent SIA tensors can compete with the leading exchange to promote noncollinearity [24], yet experimental realizations of anisotropy-dominated helimagnets remain elusive.

Here, we combine comprehensive experimental characterization with first-principles calculations to investigate helimagnetism in chiral Co_5TeO_8. Our density functional theory (DFT) calculation predicted a 127-meV charge-transfer gap, motivating the synthesis and investigation of its magnetic properties. Using magnetic and thermodynamic probes, we constructed a high-resolution multi-phase diagram consisting of 8 different phases. In addition, we employ neutron scattering, high-field magnetometry, and capacitance measurements to map this magnetic landscape and characterize compact field-tunable helical textures. These experiments indicate that site-dependent SIA, rather than DMI, is the leading interaction governing the stabilization of the helical state—a scenario further supported by ab initio many-body wavefunction calculations. Together with the experimental observations, these results suggest a framework for engineering compact magnetic textures in correlated oxides, with potential implications for magneto-electric (ME) spintronics.

Results

Strong electronic correlations in Co_5TeO_8

To search for magnets with enhanced SIA, we turned our attention to Co-based systems, targeting spinel-type Co_5TeO_8. Although its magnetic ground state depends on structural polymorphism [25], we focused on the chiral cubic phase ($P4_132/P4_332$), where geometric frustration and broken inversion symmetry enable complex magnetic textures. The combination of these structural features with Co_5TeO_8's partially filled *d*-orbitals, likely involving strong electronic correlations, motivated us to investigate its electronic structure.

To assess the metallic versus insulating character of its electronic structure, we performed DFT calculations within the local density approximation (LDA) + *U* framework, using the experimental crystal structure (see Fig. 1A). The LDA + *U* approach, incorporating on-site Coulomb repulsion via a Hubbard *U* parameter, has successfully reproduced band gaps in Mott insulators such as Na_2IrO_3 [26]. For Co_5TeO_8, while standard LDA predicts metallic behavior, introducing $U = 3$ eV opens a charge-transfer gap of 127 meV at the Γ-point (Fig. S1), a result robust to the choice of *U*. The predominant *d*-character of the bands near the Fermi energy indicates strong electronic correlations, implying sensitivity to external fields and potential ME coupling.

To explore magnetism of Co_5TeO_8, we synthesized a high-quality microcrystalline sample and performed comprehensive structural characterization. Structural analysis confirms that Co_5TeO_8 crystallizes in the chiral space group $P4_332$ (or its enantiomorph $P4_132$), with both inequivalent magnetic Co sites adopting a 2+ oxidation state as confirmed from electron energy loss spectroscopy (EELS) measurements (Section S2). Further structural details are provided in Section S1. The Co1 sublattice (12*d* sites) forms corner-sharing triangular motifs that interconnect with Co2 ions (8*c* sites) to complete a 3-dimensional framework of corner-sharing tetrahedra. This geometry generates strong magnetic frustration where competing exchange interactions between the 2 sublattices may suppress conventional magnetic order [27]. The combination of strong electronic correlations on the chiral frustrated lattice establishes Co_5TeO_8 as a platform for hosting nontrivial magnetic textures. As we demonstrate in the following sections, localized 3*d* electrons in Co_5TeO_8 enable tunable magnetic phenomena with a rich phase diagram.

Complex field-tunable magnetic phase diagram

High-resolution magnetometry reveals a complex magnetic energy landscape in Co_5TeO_8 with multiple phase transitions, as shown in Fig. 1C. The real component of ac susceptibility (χ'_{ac}) exhibits a sharp peak at 44.9 K (T_{HM}), indicating onset of long-range magnetic order in phase I (see Fig. 2A). This transition displays clear dissipative character, as evidenced by a corresponding peak in imaginary susceptibility (χ''_{ac}). Below T_{HM}, 2 additional hysteretic regions emerge at $T^{(1)}_{hys}$ and $T^{(2)}_{hys}$, consistently observed in both ac susceptibility and dc magnetization. Applied magnetic fields cause these transitions to converge and shift toward T_{HM} (Fig. 2C and Section S3), suggesting renormalization effects similar to skyrmion lattice hosts [28–30].

Heat capacity measurements reveal contrasting thermodynamic signatures. While magnetometry shows pronounced features at all 3 transitions, heat capacity exhibits only weak anomalies at T_{HM} and $T^{(2)}_{hys}$, with no discernible signature at $T^{(1)}_{hys}$ (see Fig. 2B). This suppressed response despite clear magnetic signatures suggests minimal entropy changes governed by persistent short-range correlations, previously identified in Ref. [25]. Field-dependent magnetometry data reveal pronounced metamagnetic transitions below T_{HM}, becoming increasingly steeper at lower temperatures with broadened hysteresis, as shown in Fig. 2D. These field-driven responses coincide with sharp anomalies in electrical capacitance (Fig. 2E, inset, and Section S3), confirming ME coupling in Co_5TeO_8, which is crucial for functional control. Remarkably, magnetic saturation is absent even at 60-T pulsed fields (Fig. 2E), presumably reflecting frustration in the strongly-coupled tetrahedral framework where competing exchanges prevent forced ferromagnetic alignment [31]. This intricate behavior necessitates comprehensive neutron scattering to resolve the underlying magnetic structure.

Compact spiral order revealed by neutron scattering

To uncover the magnetic structure in Co_5TeO_8, we performed powder neutron diffraction (PND) measurements. Just below T_{HM}, magnetic satellites emerge around (*h*,*h*,*h*) and (*h*,*h*,0) nuclear reflections (see Fig. 3A), characterized by incommensurate propagation vectors $\boldsymbol{Q}^{1a}_{IC} = \boldsymbol{G}_{111} \pm \boldsymbol{q}^{(1)} = \boldsymbol{G}_{110} \pm \boldsymbol{q}^{(1)}$, consistent with a previous report [25]. Notably, no magnetic satellites appear around $\boldsymbol{G}_{h00}$ reflections within instrumental resolution. The systematic absences of (*h*,0,0) reflections ($h \neq 4n$) confirm that the 4_1 (or 4_3) screw symmetry of the parent space group is retained, although overall cubic magnetic symmetry is broken by incommensurate modulation.

Small-angle neutron scattering (SANS) measurements provide complementary information about the magnetic order. Due to powder averaging, the discrete incommensurate $\boldsymbol{Q}$-vectors manifest as ring-like scattering patterns on the 2-dimensional multidetector. Figure 3B and C show data at 44 and 2 K, respectively. The ring-like scattering centered at the Γ-point corresponds to $\boldsymbol{Q}^{(1)}_{IC}$ with $|\boldsymbol{Q}| = 0.903(2)$ nm^{-1} at T_{HM} and $\boldsymbol{Q}^{(2)}_{IC}$ with $|\boldsymbol{Q}| = 1.1(1)$ nm^{-1} below $T^{(2)}_{hys}$ (Fig. 3D). The corresponding pitch length at 2 K is $\lambda_h = 5.71 \pm 0.51$ nm, increasing with temperature from λ_h (T_{HM}) = 6.96 ± 0.02 nm to λ_h ($T^{(1)}_{hys}$) = 9.66 ± 0.15 nm.

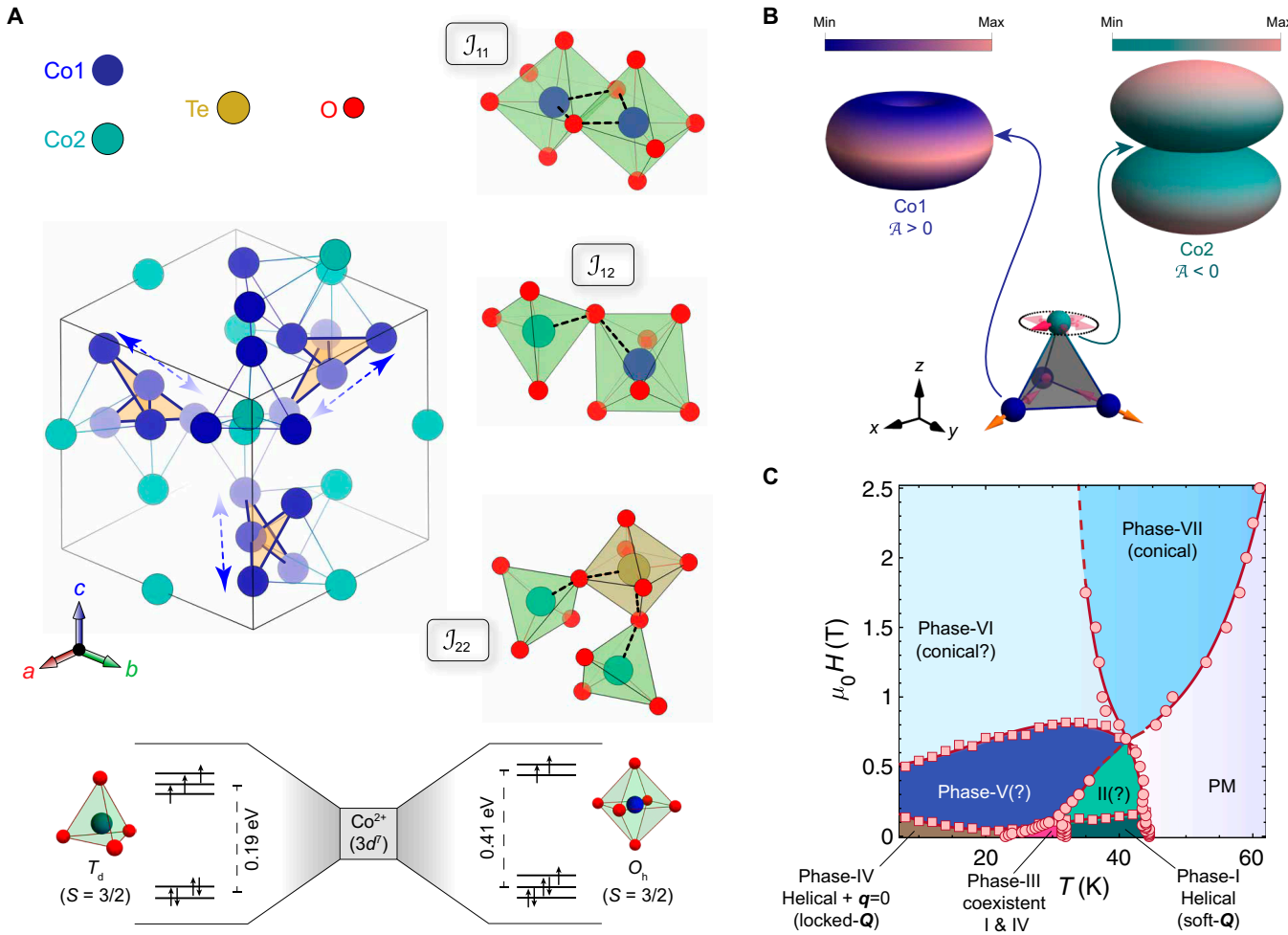


Fig. 1. Phase diagram and local magnetic anisotropy of chiral cubic Co_5TeO_8. (A) Crystal structure of Co_5TeO_8 viewed slightly away from [111] axis, consisting of 2 inequivalent Co ions: Co1 in blue and Co2 in teal. For simplicity, Te and O atoms are omitted from the full unit cell depiction. The dashed double arrows represent the Co1 ions arranged along ⟨110⟩, which form triangular plaquettes (shaded yellow). Two corner-sharing plaquettes are mutually rotated by 110° with respect to each other. Ultimately, they form corner-sharing tetrahedra with Co2 ions. The connectivity of various Co–O polyhedra are shown, with nearest-neighbor (NN) and next-nearest-neighbor (NNN) superexchange pathways represented by dashed lines. Here, $\mathcal{J}_{11}$, $\mathcal{J}_{12}$, and $\mathcal{J}_{22}$ represent bilinear exchanges between Co1–Co1, Co1–Co2, and Co2–Co2 sites, respectively. Crystal electric field splitting diagrams of Co^{2+} ions in tetrahedral and octahedral environments are depicted. (B) Ab initio calculations indicate contrasting single-ion anisotropies ($\mathcal{A}$), identifying the Co1 sublattice as having easy-axis character and the Co2 sublattice as easy-plane. Consequently, the schematic depicts Co1 spins pointed along the local ⟨111⟩ axes, with Co2 spins constrained within the plane orthogonal to the local z axis. (C) Magnetic phase diagram of Co_5TeO_8 constructed from high-resolution $M(H)$ and $\chi_{ac}(T)$ data. We identify up to 8 distinct phases in the explored parameter space. Filled circles and rectangles represent phase boundaries extracted from $\chi_{ac}(T)$ and $M(H)$ data, respectively. These data can be found in Fig. 2 and Figs. S5 and S6. For magnetic field-dependent phase boundaries, we only consider data obtained while the field is ramped up. SANS analysis indicates that the helical wavevector is locked at $Q = 1.1(1)$ nm^{-1} in phase IV, whereas it exhibits a monotonic change of its magnitude in phase I ("soft-$\boldsymbol{Q}$"). In phase II, the scattering intensity is distributed along an arc with constant angular width and linearly decaying intensity, eventually evolving into the characteristic 2-spot pattern of the conical state (phase VII). See Fig. 4 and main text for further details.

These compact magnetic periodicities are among the shortest reported in chiral insulator magnets. See Table 1 for a thorough comparative list of most-relevant noncentrosymmetric magnets. However, the unpolarized neutron scattering measurements alone cannot distinguish between different spiral helicities. To determine whether these ultracompact spirals adopt proper-screw or cycloidal character, we performed polarization-analyzed SANS measurements as described in the following section.

Bloch-type modulation deduced from polarized SANS

Having established the compact spiral order, we performed uniaxial polarization-analyzed SANS to determine the helical spin texture. A schematic of the experimental setup is shown in Fig. 3E. The incoming neutron polarization vector is aligned (or anti-aligned) with the neutron beam. Non-spin-flip (NSF) and spin-flip (SF) scattering cross-sections are probed using a spin state analyzer placed between sample and detector. This configuration enables the decomposition of the magnetic interaction vector $m_{\perp}(\boldsymbol{Q})$ into components defined by the polarization axis. The NSF cross-section isolates the projection of $m_{\perp}(\boldsymbol{Q})$ parallel to the initial polarization P_i (as indicated in Fig. 3E), whereas the SF channel is sensitive to the component simultaneously orthogonal to both P_i and $\boldsymbol{Q}$. Consequently, for a helimagnetic spiral characterized by moments distributed isotropically in the plane normal to $\boldsymbol{Q}$, the scattering intensity is expected to be equally distributed between the NSF and SF channels. In contrast, for an easy-plane cycloidal structure with

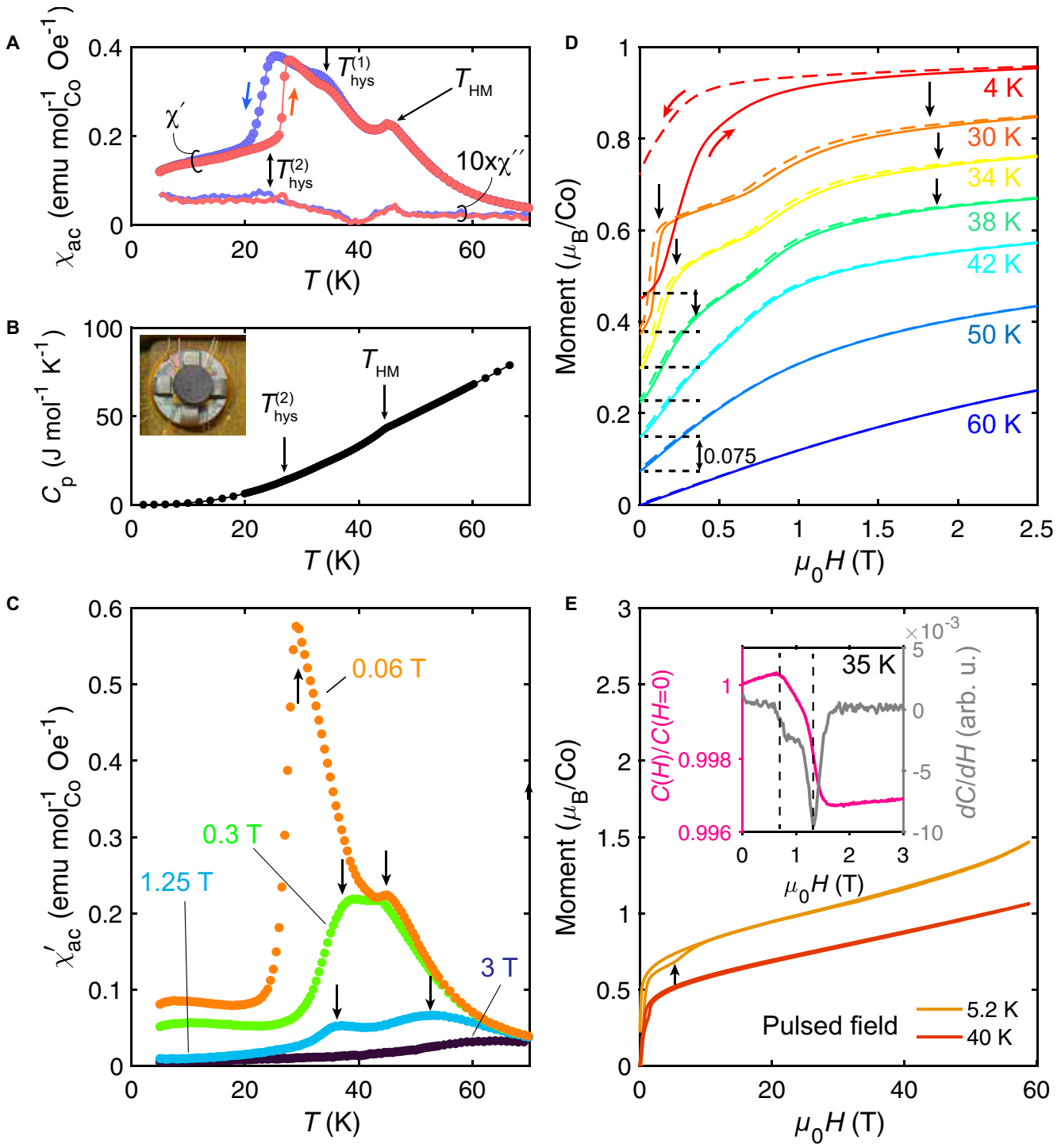


Fig. 2. Magnetic and thermodynamic response across the multi-phase diagram of magnetoelectric Co_5TeO_8. (A) Result of ac susceptibility measurement on Co_5TeO_8 polycrystalline powder in zero field. A constant factor of 10 has been applied to the imaginary part (χ''_{ac}) of the total susceptibility for better visualization. (B) Specific heat data collected in zero field shows a weak anomaly at T_{HM}. Inset shows the pressed pellet ($\phi \sim 3.2$ mm) used for these measurements. (C) Ac susceptibility data as a function of temperature measured at 4 different magnetic fields, scanning across various transitions. (D) Magnetization evolution as a function of magnetic field at 7 different temperatures selected according to the phase diagram shown in Fig. 1C. (E) High pulsed magnetic field data of Co_5TeO_8 collected at 2 temperatures show no sign of saturation magnetization up to 60 T. Inset shows evolution of capacitance (C), and the corresponding dC/dH, as a function of external magnetic field at a fixed temperature of 35 K. The dashed vertical lines are the phase boundaries extracted earlier. Black arrows in all panels mark the occurrence of temperature (or magnetic field)-induced transitions.

moments confined to the $\boldsymbol{Q}$–x (or $\boldsymbol{Q}$–z) plane, the magnetic scattering is expected to appear exclusively in the NSF (or SF) channel, respectively. See Ref. [32, 33] for more details. Since the ring-like scattering pattern (Fig. 3F) represents a superposition of multiple magnetic domains, each angular segment provides equivalent information about NSF and SF cross-sections, enabling systematic analysis across different $\boldsymbol{Q}$-vector orientations.

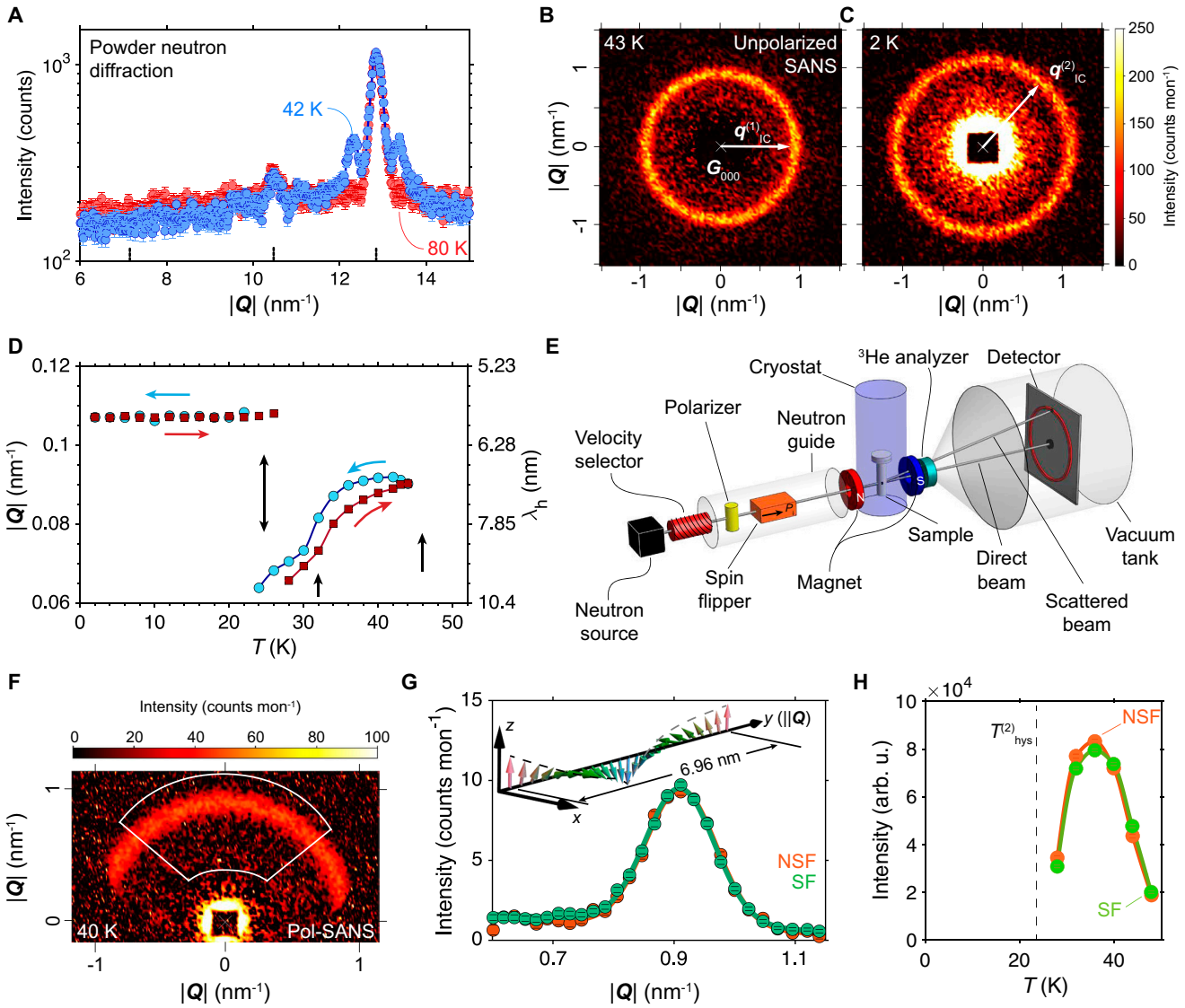


Fig. 3. Compact helimagnetic order revealed by neutron scattering. (A) Wide-angle neutron diffractograms of Co_5TeO_8 obtained at 2 temperatures above and below T_{HM}, focused on 2 reflections of the principal cubic directions, show appearance of magnetic satellites around them. The nuclear reflections (from low- to high-Q: (100), (110), and (111)) are marked by dashed vertical lines. We do not observe any incommensurate (IC) satellites around the forbidden (001) reflection. (B and C) SANS 2D detector image obtained just below T_{HM} and at $T = 2$ K, respectively. The circular distribution of the magnetic scattering intensity is consistent with the expectation for magnetic scattering arising at propagation vector q within randomly oriented grains of the polycrystalline sample. (D) Length of incommensurate magnetic wavevectors (and the corresponding pitch length of the spiral in real space, λ_h) as a function of temperature. Phase boundaries, as obtained from our χ_{ac} data, have been clearly marked by vertical arrows. (E) Schematic of the uniaxial polarization analysis setup employed at D33 to investigate the IC state in Co_5TeO_8. A uniform longitudinal guide field was applied along the incoming beam direction in order to maintain the polarization of the incoming beam. Representative detector image is also sketched, with a characteristic circular magnetic scattering pattern. The setup for unpolarized SANS measurements is similar, but with polarizer, spin flipper, and analyzer removed. (F) Representative detector image obtained at $T = 40$ K. Polarization analysis was performed only on the scattered neutrons forming the upper arc on the detector (inside the white sector box). Due to the analyzer's finite size, only scattering within the top portion of the detector could be analyzed. (G) Integrated intensity of NSF and SF polarized SANS signals observed in phase I at 40 K. Equal NSF and SF scattering intensities are consistent with a Bloch-type modulation. Inset shows a real-space sketch of the proper helical magnetic structure realized in Co_5TeO_8. The indicated pitch length of the helix is the one obtained at 44 K, just below T_{HM}. (H) Evolution of NSF-SF scattering intensity between T_{HM} and $T^{(2)}_{hys}$.

Analysis of polarized SANS data at 40 K shows nearly equivalent intensities in both NSF and SF channels for phase I (Fig. 3G). This balanced contribution indicates that magnetic Fourier components lie predominantly in the plane perpendicular to $\boldsymbol{Q}$ with comparable amplitudes in both horizontal and vertical directions, consistent with helimagnetic spiral arrangement (schematic shown in inset of Fig. 3G). The helicity is retained down to $T^{(2)}_{hys}$ as deduced from equal NSF-SF intensities (Fig. 3H). More detailed analysis using narrower sector boxes reproduces the same result (Section S4). While helical modulation is expected due to the chiral crystal structure, the unusually short magnetic period sharply differentiates Co_5TeO_8 from archetypal DM-stabilized helimagnets [34–36]. Having confirmed the Bloch-type helical character, we next investigate how applied magnetic fields modify the helical pitch and induce phase transitions, as revealed by field-dependent SANS measurements.

Table 1. List of noncentrosymmetric magnets hosting incommensurate spin textures. Here, DMI and RKKY refer to Dzyaloshinskii–Moriya interaction and Ruderman–Kittel–Kasuya–Yosida interaction, respectively. "DMI-based" refers to where DM interaction competes with leading order exchange to stabilize the incommensurate ground state. Superscripted "c" stands for the electrically conducting members from the list of compounds. Note that some systems, such as $EuNiGe_3$, may possess both Bloch- and Néel-type twisting, aptly designated by "mixed" helicity.

Material	Space group	Pitch length	Helicity	Stabilization mechanism	Reference
$EuNiGe_3$[c]	*I*4*mm* (107)	1.7 nm	Mixed	RKKY + DM interaction	[64]
EuPtSi[c]	$P2_13$ (198)	1.8 nm	Bloch	Geometric frustration + DM + RKKY + four-spin interactions	[65]
MnGe[c]	$P2_13$ (198)	2.8–5.5 nm	Bloch	Exchange frustration	[66]
$YbNi_3Al_9$[c]	*R*32 (155)	3.4 nm	Bloch	RKKY + DMI	[67]
$Ba_3NbFe_3Si_2O_{14}$	*P*321 (150)	3.7 nm	Bloch	Exchange frustration	[68]
Co_5TeO_8	***P*4$_3$32/*P*4$_1$32 (212/213)**	**5.7–10 nm**	**Bloch**	**SIA + DMI + Frustration**	**This work**
CeAlGe[c]	$I4_1md$ (109)	6 nm	Néel	RKKY + DMI	[69]
$Y_3Co_8Sn_4$[c]	$P6_3mc$ (186)	8–16 nm	In-plane vortex	Four-spin interaction	[70]
$Pr_5Ru_3Al_2$[c]	$I2_13$ (199)	15 nm	Bloch	DMI-based	[71]
Ni_2InSbO_6	*R*3 (146)	15.7 nm	Bloch	DMI-based	[72]
MnSi[c]	$P2_13$ (198)	17 nm	Bloch	DMI-based	[73]
$Ba_2CuGe_2O_7$	$P\bar{4}2_1m$ (113)	22 nm	Bloch	DMI-based	[74]
$GaV_4(S/Se)_8$	*R*3m (160)	22 nm	Néel	DMI-based	[75]
$CrTa_3S_6$[c]	$P6_322$ (182)	22.5 nm	Bloch	DMI-based	[76]
$Fe_{1-x}Co_xSi$[c]	$P2_13$ (198)	30–200 nm	Bloch	DMI-based	[77]
$Cr_{1/3}NbS_2$[c]	$P6_322$ (182)	48 nm	Bloch	DMI-based	[78]
Cu_2OSeO_3	$P2_13$ (198)	62 nm	Bloch	DMI-based	[35]
$BiFeO_3$	*R*3*c* (161)	62 nm	Néel	DMI-based	[79]
FeGe[c]	$P2_13$ (198)	70 nm	Bloch	DMI-based	[80]
$Co_xZn_yMn_z$[c]	*P*4$_3$32/*P*4$_1$32 (212/213)	70–130 nm	Bloch	DMI-based	[51]
$FeCo_{0.5}Rh_{0.5}Mo_3N$	*P*4$_1$32 (213)	110 nm	Bloch	DMI-based	[81]
$NdFe_3(BO_3)_4$	*R*32 (155)	114 nm	Bloch	DMI-based	[82]
$VOSe_2O_5$	*P*4*cc* (103)	125–180 nm	Néel	DMI-based	[83]
$Mn_{1.4}Pt_{0.9}Pd_{0.1}Sn$[c]	$I\bar{4}2m$ (121)	>130 nm	Mixed	Dipolar + anisotropic DMI	[84]
$Fe_{1.9}Ni_{0.9}Pd_{0.2}P$[c]	$I\bar{4}2m$ (121)	280 nm	Mixed	Dipolar + anisotropic DMI	[85]

Field-driven transformation of the helimagnetic spiral

To investigate the magnetic field response of the incommensurate phases, we systematically tracked the evolution of $\boldsymbol{Q}_{\mathrm{IC}}^{(1)}$ under applied transverse magnetic fields ($\mu_0 H \perp k_i$) using SANS. Starting from zero-field ring-like scattering at 36 K in phase I (Fig. 4A), applied magnetic field gradually transforms the ring into an intermediate phase characterized by arcs of scattering (Fig. 4B) before entering a well-defined conical phase at higher fields (Fig. 4C). The conical phase is clearly identified by a pair of spots with propagation vectors aligned parallel and antiparallel to the applied field, consistent with other cubic helimagnets [34,35]. Further field increase suppresses incommensurate satellites above 2.5 T, leading to field-polarized magnetic order. Notably, the absence of scattering intensity in sectors perpendicular to the applied field (around $\psi = 0°$ or 180° in Fig. 4D and teal sector box in Fig. 4E) definitively excludes formation of the conventional multi-$\boldsymbol{Q}$ skyrmion lattice observed in other chiral cubic magnets.

The intermediate phase (phase II) exhibits distinctive characteristics revealing complexity of underlying magnetic interactions. Unlike the conical phase with monotonic peak-width decay, the intermediate phase maintains nearly constant azimuthal intensity distribution across its stability range (Fig. 4E, inset). This behavior suggests stabilization of a multi-domain incommensurate structure with $\boldsymbol{Q}$-vectors distributed between ⟨110⟩ and ⟨111⟩ directions, with the field only partially selecting preferred orientations. Remarkably, the incommensurate wavevector magnitude $|\boldsymbol{Q}^{(1)}|$ increases systematically with applied field (see Fig. 4F), indicating that the spiral shortens under field rather than collapsing into ferromagnetic-type alignment. This field-driven reduction of helical pitch is rare among DMI-stabilized helimagnets, necessitating ab initio wavefunction-based calculations to understand microscopic magnetic interactions.

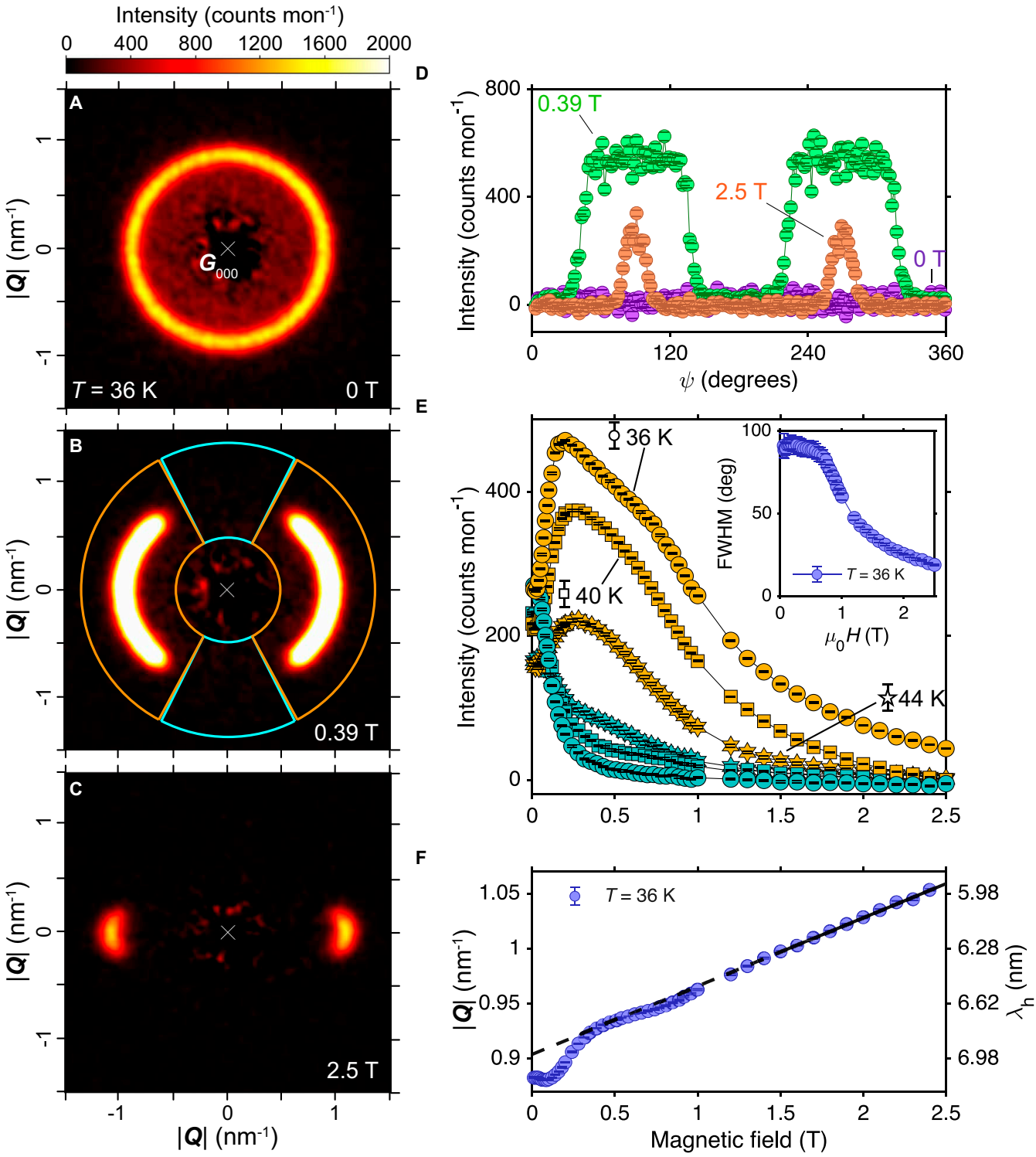


Fig. 4. Evolution of the helimagnetic spiral in transverse magnetic field. (A to C) Detector images obtained in a magnetic field of 0, 0.39, and 2.5 T at $T = 36$ K. The incident neutron beam is directed perpendicular to the detector plane, while the magnetic field is applied transverse to it (horizontal in the detector images). (D) Corresponding azimuthal scans at the 3 magnetic field values. For clarity, a constant offset of −250 counts/mon is applied to the data at 0 T. (E) Magnetic field dependence of the scattering intensities extracted from the orange and cyan sector boxes indicated in (B). The inset displays the full width at half maximum (FWHM) of the azimuthal intensity arcs as a function of magnetic field at $T = 36$ K. (F) Field evolution of the incommensurate component of the magnetic order (Q), together with its corresponding pitch length in real space. Data above 1.5 T are fitted to illustrate the linear scaling of $|Q(H)|$ and the corresponding λ_h.

SIA-dominated magnetic energy landscape

The Co–O coordination geometries in Co_5TeO_8 deviate significantly from ideal octahedral and tetrahedral environments with ∠Co1–O–Co1 and ∠Co2–O–Co2 bond angles of 94.51(1)° and 116.77(1)°, respectively. These distortions make prediction of exchange interactions via Goodenough–Kanamori–Anderson

rules challenging, thus requiring explicit quantum chemistry calculations. Hence, we employed electrostatically embedded finite-size clusters extracted from the experimental crystal structure (see Fig. 1A), an approach well-suited for strongly correlated *d*-electron systems with highly localized electronic states [37–42]. We used the following spin Hamiltonian encompassing both on-site and intersite magnetic interactions:

$$\mathcal{H} = \sum_{\langle ij\rangle=1,2} \mathcal{J}_{ij}\left(S_i \cdot S_j\right) + \mathcal{K}_{ij}\left(S_i \cdot S_j\right)^2 + \mathcal{D}_{ij} \cdot \left(S_i \times S_j\right) + \sum_i \mathcal{A}_i \left(S_i \cdot \hat{e}_i\right)^2 \quad (1)$$

The summation $\langle i, j\rangle$ runs over all nearest-neighbor bonds. The exchange parameters: bilinear ($\mathcal{J}_{ij}$), biquadratic ($\mathcal{K}_{ij}$), and antisymmetric DM interaction vectors ($\mathcal{D}_{ij}$ (11, 12)) are bond-type-dependent, taking 3 distinct sets of values corresponding to Co1–Co1 ($\mathcal{J}_{11}$, $\mathcal{K}_{11}$, $\mathcal{D}_{11}$), Co2–Co2 ($\mathcal{J}_{22}$, $\mathcal{K}_{22}$, $\mathcal{D}_{22}$), and Co1–Co2 ($\mathcal{J}_{12}$, $\mathcal{K}_{12}$, $\mathcal{D}_{12}$) bonds, as shown in Fig. 1A. $\mathcal{A}_i$ is the SIA coefficient for site *i*, where $\hat{e}_i$ represents the site-dependent anisotropy axis. Further details about our quantum chemistry calculations can be found in the Methods section and Section S5.

We find that all 3 bilinear exchange pathways are antiferromagnetic with $\mathcal{J}_{11} = 0.116$ meV, $\mathcal{J}_{22} = 0.088$ meV, and $\mathcal{J}_{12} = 0.208$ meV (see Table S2), at least 20 times weaker than the thermal energy scale ($k_B T_{HM} \sim 3.9$ meV) associated with T_{HM}, suggesting that the bilinear exchanges alone underestimate the long-range ordering temperature. The biquadratic interactions, in turn, are ferromagnetic-type with $\mathcal{K}_{11} = -8.4$ μeV, $\mathcal{K}_{22} = -1.11$ μeV, and $\mathcal{K}_{12} = -3.2$ μeV, representing 5% to 8% of the corresponding bilinear strengths. Remarkably, the Co1–Co1 bonds exhibit exceptionally large DMI, with $|\mathcal{D}| = 0.099$ meV yielding $|\mathcal{D}/\mathcal{J}| \simeq 0.84$, atypical for insulating chiral oxides, while Co2–Co2 bonds show negligible DMI ($|\mathcal{D}/\mathcal{J}| \simeq 0.03$) and Co1–Co2 bonds display intermediate values ($|\mathcal{D}/\mathcal{J}| \simeq 0.102$). As schematically shown in Fig. 1B, the calculated SIA constants are site-dependent, with $\mathcal{A}_1 = -2.1$ meV (easy-axis along [111] for Co1 at 12*d* sites) and $\mathcal{A}_2 = 3.1$ meV (*xy*-easy-plane for Co2 at 8*c* sites), representing the dominant energy scale, approximately 10 to 15 times larger than exchange interactions. In the absence of strong anisotropy in a single sublattice system without interaction, the canonical DMI helimagnet relation $\lambda_h = 4\pi\mathcal{J}a/\mathcal{D}$ predicts $\lambda_h \simeq 5.3$ nm for Co1–Co1, coincidentally close to the observed range of 5.7 to 9.6 nm across the temperature-dependent phases. The same relation predicts $\lambda_{Co1\text{–}Co2} \simeq 45$ nm and $\lambda_{Co2\text{–}Co2} \simeq 109$ nm, both incompatible with experimental observations. The calculated energy hierarchy $\mathcal{A} \gg \mathcal{J} > \mathcal{D} \gg \mathcal{K}$, combined with competing antiferromagnetic exchanges on the 2-sublattice spinel-like structure, identifies Co_5TeO_8 as a frustrated magnetic system in which the SIA exceeds the exchange and DMI. In this regime, frustration and DMI drive the underlying finite-$\boldsymbol{Q}$ instability and chirality, while the dominant site-dependent SIA is proposed to lift the directional degeneracy and to favor a propagation vector selected from the otherwise nearly degenerate manifold.

This counterintuitive strong SIA can be traced to the electronic structure of high-spin Co^{2+} (d^7, $S = 3/2$) in distinct local environments. For the octahedral Co1 sites (12*d*, $t_{2g}^5 e_g^2$), the incompletely filled t_{2g} manifold is expected to retain unquenched orbital angular momentum, in contrast to either fully filled or half-filled configurations. The Co1 octahedron exhibits a local ⟨111⟩-oriented distortion where the 6 Co–O coordinations comprise 2 short (2.01 Å), 2 intermediate (2.14 Å), and 2 long (2.17 Å) bond lengths, with the 2 short bonds subtending an expanded angle of 97.3° and the 2 long bonds subtending a contracted angle of 86.3°, consistent with compression along the pseudo-3-fold axis. This distortion splits the parent $^4T_{1g}$ term into $^4A_{2g}$ and ^4E_g components in D_{3d} symmetry. Mixed with spin-orbit coupling, this split manifold produces zero-field splitting of the $S = 3/2$ states with easy-axis character along the compression direction, yielding in our calculation $\mathcal{A}_1 = -2.1$ meV [43,44]. In contrast, the tetrahedrally coordinated Co2 (8*c* sites, $e_g^4 t_{2g}^3$) presents a distinct scenario. The $^4A_2$ ground term of tetrahedral Co^{2+} is an orbital singlet with no first-order orbital angular momentum. Nevertheless, Co2 occupies a trigonally compressed tetrahedron (C_{3v} symmetry) with one short Co–O bond (1.91 Å) along the 3-fold axis and 3 longer bonds (2.02 Å), yielding O–Co–O angles of 106.6° and 112.2°. This distortion modifies both the energies and symmetries of the excited-state manifold (primarily $^4T_2$) that couples to the ground state via spin-orbit interaction. Our ab initio calculations indicate that this second-order mechanism produces easy-plane anisotropy ($\mathcal{A}_2 = 3.1$ meV), whose magnitude appears to be enhanced by covalent mixing with heavy tellurium ligands. This overlap is expected to increase the effective spin-orbit coupling at Co2 sites and amplifies these second-order contributions despite the absence of first-order orbital effects. The insulating state with persistent correlations in Co_5TeO_8 is likely essential for preserving this strong SIA. In itinerant systems, electron delocalization into broad conduction bands quenches orbital angular momentum and averages over local distortions, substantially reducing magnetic anisotropy. This suppression is evidenced by the 4-fold reduction in near-metallic CoV_2O_4 compared to the wider-gap isostructural Mott insulator MnV_2O_4, where electron localization preserves the orbital physics [45–47]. The combination of Te-induced distortions at both Co sites, unquenched orbital moments at Co1, heavy-ligand spin-orbit enhancement at Co2, and Mott localization preserving the local electronic structure is proposed to produce the dominant site-dependent SIA.

Discussion

The microscopic origin of sub-10-nm helimagnetism in Co_5TeO_8 presents a compelling materials physics puzzle: In the absence of strong anisotropy, canonical DMI helimagnets achieve $\lambda_h \sim 18$ to 130 nm, yet Co_5TeO_8 realizes $\lambda_h \sim 5.7$ to 9.6 nm despite only moderately enhanced $|\mathcal{D}/\mathcal{J}|$ compared to archetypal chiral magnets (e.g., MnSi ~ 0.12 [48]; Cu_2OSeO_3 ~ 0.04 to 0.58 [31]). Our ab initio calculations point to a different mechanism in which site-dependent SIA, an order of magnitude larger than all exchange interactions, provides the leading energy scale. Three competing antiferromagnetic exchanges on the 2-sublattice structure create geometric frustration, producing a nearly flat $E(\boldsymbol{Q})$ landscape over 0.8 to 1.3 nm^{-1}. Within this degenerate manifold, dominant SIA is proposed to select the helical wavevector through $\boldsymbol{Q}$-dependent orientational averaging, where shorter wavelengths reduce anisotropy penalties by allowing larger intersite spin canting that better accommodates the conflicting easy-axis (Co1) and easy-plane (Co2) local environments. While the canonical $\lambda_h = 4\pi\mathcal{J}a/\mathcal{D}$ relationship using Co1–Co1 parameters coincidentally predicts $\lambda_h \sim 5.2$ nm, this numerical agreement may mask distinct physics: Large DMI

creates the helical instability and establishes chirality, but we argue that SIA provides the leading contribution to wavelength selection within the frustrated landscape. This SIA-selection mechanism is supported by T- and H-dependent neutron scattering data, detailed below. Additionally, weak ferromagnetic-type biquadratic interactions (5% to 8% of bilinear strength) lift residual degeneracies within the frustrated $\boldsymbol{Q}$-space manifold and provide energy barriers between competing helical variants, enabling sharp phase transitions and hysteretic behavior. Although individual exchange bonds are modest, the experimentally observed T_{HM} is driven by collective stabilization from the full frustrated lattice and strong anisotropy, as captured by mean-field analysis (Section S5). This mechanism is intrinsically tied to the predicted insulating ground state with strong electronic correlations, which favors the localized orbital physics underlying the enhanced SIA while maintaining sufficient correlation strength to generate competing exchange pathways. In summary, Co_5TeO_8 thus appears to realize a DMI-initiated, SIA-enhanced, frustration-enabled compact helimagnet and may serve as a prototype for a class of anisotropy-dominated helimagnets in strongly correlated insulators.

Another indication of SIA dominance emerges from the field dependence of the helical wavevector. Co_5TeO_8 exhibits field-driven compression ($d\boldsymbol{Q}/dH > 0$ as shown in Fig. 4F), not what is expected from canonical DMI helimagnets for which the modulation period is typically field independent to first approximation. In Co_5TeO_8, the field reorients the spin configuration, and on the frustrated 2-sublattice landscape, this favors shorter helical pitches that better accommodate the conflicting easy-axis (Co1) and easy-plane (Co2) environments. This distinctive field response is difficult to reconcile with a purely DMI-controlled wavelength selection and is most naturally explained if SIA provides the leading contribution. The synergy between frustration and SIA manifests dramatically in high-field magnetization, which fails to saturate even at 60 T ($E_{Zeeman} \sim 10.4$ meV), as shown in Fig. 2E. This nonsaturation arises from geometric frustration creating competing exchange fields that reduce the effective molecular field, while calculated SIA barriers (~24 T for Co1, ~36 T for Co2) must be overcome to fully polarize spins. The contrasting anisotropy character of the 2 sublattices, combined with competing interactions, underlies the rich 8-phase magnetic diagram, where phase boundaries reflect competition between helical wavevector selection, rotation plane orientation, and Co1–Co2 sublattice coupling. Further experiments on Co_5TeO_8 single crystals combined with theoretical modeling are required to validate these points.

The SIA-dominated mechanism is further supported by 2 distinct temperature-induced features. First, at T_{HM}, long-range helical order emerges with a temperature-dependent wavevector $|\boldsymbol{Q}(T)|$ that evolves as thermal fluctuations partially quench the effective anisotropy. Second, upon cooling through a first-order lock-in transition at T_{lock} ($= T_{hys}^{(2)} \sim 25$ K) exhibiting substantial thermal hysteresis (Fig. 2A), the helical period becomes temperature independent and rigidly fixed at $\lambda_h = 5.7$ nm. The energy scale $k_B T_{lock} \sim 2.15$ meV is comparable to the calculated Co1 single-ion barrier $\mathcal{A}_1$ (also naturally lower than $\mathcal{A}_2$), suggesting that reduction of thermal energy below this scale may trigger the transition and pins the system in the SIA-optimized configuration. This 2-transition phenomenology bears striking similarity to the archetypal Ising chain material $CoNb_2O_6$, which also exhibits an incommensurate–commensurate lock-in [49], but with a fundamental mechanistic difference. In $CoNb_2O_6$, ultra-strong crystal-field splitting (~30 meV) quenches the spin to $S_{eff} = 1/2$ and rigidly locks spin directions along a single axis, permitting only amplitude modulation of collinear ferromagnetic chains in the intermediate phase; lock-in is then driven by weak interchain coupling, occurring at an energy scale much smaller than the crystal-field splitting. In contrast, Co_5TeO_8's moderate SIA preserves $S = 3/2$ and permits continuous spin rotation, resulting in helimagnetic spiral, with lock-in occurring at $T_{lock} \sim \mathcal{A}_1/k_B$ via anisotropy saturation rather than interchain coupling. The hysteretic first-order character in Co_5TeO_8 points to an energy landscape with multiple metastable $\boldsymbol{Q}$-states separated by nucleation barriers, consistent with the frustrated $E(\boldsymbol{Q})$ manifold. Above T_{lock}, the system occupies a thermally accessible "soft" $\boldsymbol{Q}$-state with broader distribution, while below T_{lock}, it nucleates into a "locked" $\boldsymbol{Q}$-state with narrow, rigid distribution. This comparison supports the picture of SIA-dominated helical behavior with sufficient DMI and frustration in Co_5TeO_8, fundamentally distinct from DMI-controlled systems with monotonic changes in helical period [50].

The calculated anisotropy in Co_5TeO_8 places it in an intermediate regime within the broader landscape of chiral magnetism. At one extreme, archetypal cubic chiral magnets with weak magnetocrystalline anisotropy preserve near-degeneracy among multi-$\boldsymbol{Q}$ propagation vectors, enabling continuous $\boldsymbol{Q}(T)$ evolution and field-stabilized skyrmion lattices; metallic MnSi, $Fe_{1-x}Co_xSi$, and the insulating Cu_2OSeO_3 exemplify this regime. At the opposite extreme, $CoNb_2O_6$'s ultra-strong anisotropy restricts magnetic modulation to amplitude fluctuations of collinear order, suppressing all noncollinear textures and enforcing rigid uniaxial Ising behavior. Co_5TeO_8 lies between these limits where site-dependent SIA dominates exchange by at least an order of magnitude, yet remains small enough in absolute terms to preserve unquenched $S = 3/2$ and permit continuous spin rotation. Unlike weak-anisotropy systems where higher-harmonic coupling enables multi-$\boldsymbol{Q}$ states [23], the dominant SIA in Co_5TeO_8 strongly penalizes spin textures that deviate from locally optimized easy axes defined by the chiral crystal structure. A multi-$\boldsymbol{Q}$ superposition, which inherently requires spins to point in nearly isotropic directions to satisfy multiple wavevectors, incurs higher anisotropy cost compared to a single-$\boldsymbol{Q}$ helix that can coherently adapt its phase to the local anisotropy axes [21]. Consequently, the system is driven toward a single-$\boldsymbol{Q}$ harmonic state, effectively "locking" the magnetic texture to the structural chirality and suppressing complex multi-$\boldsymbol{Q}$ topologies. The lock-in transition and field-driven helix compression described above are absent in weaker-anisotropy systems, consistent with SIA playing the leading role. The β-Mn-type $Co_8Zn_8Mn_4$, with comparable DMI but weaker anisotropy, provides direct comparison, as it exhibits a longer λ_h (Table 1) while retaining skyrmion phases, supporting the role of SIA in suppressing multi-$\boldsymbol{Q}$ skyrmion phases [51]. These findings suggest a transferable design principle: Systematically weakening SIA through selective dilution or enhancing DMI via heavier $4d/5d$ element substitution at Co^{2+} sites could generate skyrmion derivatives in isostructural compounds. More broadly, Co_5TeO_8 exemplifies how strong single-ion terms in frustrated geometries expand the accessible magnetic texture space beyond DMI paradigms, motivating exploration of anisotropy-engineered noncollinear states in other frustrated pyrochlore and spinel oxides with heavy transition metals. We note, however, that the present polycrystalline measurements do not

permit a direct experimental determination of the full anisotropy tensor; accordingly, the microscopic interaction values should be viewed as semiquantitative estimates whose main importance lies in the inferred energy-scale hierarchy.

Our work establishes Co_5TeO_8 as a magnetic insulator hosting a short-period helical ground state, with calculations indicating the presence of strong electronic correlations. The stabilization mechanism is proposed to arise from a distinctive competition between site-dependent SIA, DMI and frustration, unlike that seen in archetypal cubic helimagnets. Our results suggest a design principle that links the local coordination geometry to the nanoscale spin texture. The interplay between SIA and DMI proposed here broadens the search for short-period helimagnets beyond compounds stabilized by DMI alone, extending it to material classes with weak to moderate anisotropy. Mixed coordination structures, such as Co-based chalcogenide spinels and β-Mn-type compounds, are therefore natural candidates for systematic exploration of this mechanism. The short-period helical texture itself may find practical use in 3 areas: first, in high-frequency nano-oscillators, where the insulating ground state avoids eddy-current losses and the antiferromagnetic background cancels the Magnus force, both favoring dynamical stability [52]; second, in reservoir computing, where the 2 crystallographically distinct Co sites could provide additional nonlinear degrees of freedom compared with single-sublattice magnetic domains [53]; third, in ME switching, where the insulating ground state allows electric field rather than current-driven control—an advantage for device miniaturization, contingent on sufficiently large ME tensor elements in Co_5TeO_8 [54]. Quantitative measurement of the Mott gap and the ME coefficients will therefore be needed to assess the practical viability of voltage-controlled manipulation of the helices. Further experiments to resolve the magnon band structure of these compact helices [55], to probe nonreciprocal thermal transport arising from broken inversion symmetry [56], and to measure electric field-driven phase transitions [57] would clarify the functional potential of Co_5TeO_8 and related materials for low-dissipation spintronics. More broadly, this work suggests that competing anisotropies between inequivalent magnetic sites, usually regarded as detrimental to magnetic order, can instead serve as a design principle for engineering compact spin textures in correlated insulators.

Materials and Methods

Density functional theory calculations

Density functional theory calculations were performed using the Vienna *Ab-initio* Simulation Package (VASP) [58]. Electron-core interactions are described using the projector-augmented wave method [59], while the Kohn–Sham wavefunctions for the valence electrons were expanded in a plane wave basis with a cutoff on the kinetic energy of 400 eV. LDA + U calculations were performed within the local density approximation framework with a Coulomb on-site repulsion $U = 3$ eV acting on the d shell of Co atoms following the rotationally invariant scheme proposed by Dudarev et al. [60]. The calculations included spin-orbit coupling and noncollinear magnetism to capture the essential magnetism of Co_5TeO_8. The cubic cell ($a = 8.535$ Å) had 56 atoms, and the Brillouin zone sampling used 100 k-points with the Methfessel–Paxton smearing (width 0.01 eV). The intrinsic C_3 symmetry of the system was utilized, and static single-point energy calculations were performed without ionic relaxation. It should be noted that residual self-interaction errors inherent to LDA often result in slight underestimation of band gaps in systems with localized 3d electronic states. Thus, we may expect a slightly larger band gap in reality.

Microcrystalline sample preparation

The pure phase microcrystalline Co_5TeO_8 sample was synthesized using conventional solid-state reactions. Stoichiometric amounts of $CoCO_3$ (Aldrich, 99.999%) and TeO_2 (Aldrich, 99.999%) were thoroughly mixed using a mortar. The resultant mixture was transferred to a platinum crucible and placed inside a high-temperature muffle furnace. The temperature of the furnace was slowly raised to 1000 °C at a rate of 100 °C per hour. The furnace was then dwelled for an hour at that temperature, followed by increasing the temperature to 1100 °C at a slower rate of 50 °C per hour. The powder was then sintered at this temperature for 72 h, followed by quenching to room temperature. The quenching process was necessary to avoid co-crystallization of Co_3O_4 spinel. Results presented throughout this article were obtained on the same batch of microcrystalline sample.

Single-crystal x-ray diffraction

Microcrystalline Co_5TeO_8 grains with suitable size were mounted onto the goniometer head with cryo-loop obtained from MiTeGen, followed by installing on an Agilent SuperNOVA single-crystal diffractometer, equipped with Cu/Mo sealed tube x-ray source and an Atlas charge-coupled device detector. The temperature of the setup was controlled by an Oxford Cryostream 800 Plus system.

Electron backscatter diffraction and energy-dispersive x-ray spectroscopy measurements

We performed 2 electron backscatter diffraction (EBSD) and energy-dispersive x-ray spectroscopy (EDX) experiments. For the first experiment, Co_5TeO_8 particles were distributed over a silver-pasted stub, and EBSD spectra were collected using a field emission gun (FEG) scanning electron microscope (SEM) Zeiss Gemini 450 equipped with Oxford Instruments UltimMax EDX detector and CMOS EBSD Symmetry camera. Data acquisition was performed with the AZtec system, and subsequent processing utilized the AZtecCrystal software suite. In the second experiment, Co_5TeO_8 particles were embedded in resin and cured at 180 °C for 5 min. Prior to EBSD and EDX analysis on the same specimen, a thin carbon layer was deposited in order to reduce the electron irradiation-induced charging effects.

Magnetometry, heat capacity, and capacitance measurements

DC magnetization as well as AC susceptibility measurements were performed using the VSM and ACMS-II option of a commercial Quantum Design (QD) 14 T Physical Property Measurement System (PPMS), as well as a Magnetic Property Measurement System (MPMS), MPMS3 from QD. The polycrystalline sample was enclosed in a standard polypropylene holder provided by QD. High-field magnetization experiments were performed in pulsed magnetic fields up to $\mu_0 H = 60$ T at the Dresden High Magnetic Field Laboratory, which were normalized to laboratory measurements up to $\mu_0 H = 14$ T.

Specific heat measurements were performed on a pelletized sample. In order to produce a pellet with higher structural stability, microcrystalline sample was first crushed in a mortar for about 5 min. The diameter and height of the disc-shaped pellet

were made to be 3 and 0.5 mm, respectively. Measurements were performed using the Heat Capacity option of the 14 T PPMS, in the typical relaxation method. The pellet was mounted on the 3×3 mm^2 sapphire plate provided by QD. Apiezon-N grease was used to ensure good thermal contact between the sample and the platform. Later, the long-pulse technique was also used to measure the sample heat capacity.

Capacitance measurements were performed on a pressed Co_5TeO_8 pellet of size $5 \times 5 \times 0.5$ mm^3, using an AH2700A ultra-precision capacitance bridge in zero dc field, and with a 1-kHz excitation and a voltage of 15 V. The sample mount was installed onto 9-T PPMS. Capacitance measurements were performed as a function of magnetic field at fixed temperatures in a sweep mode.

EELS experiment

The experimental determination of the cation oxidation state in Co_5TeO_8 was carried out on a thin lamella prepared from a microcrystalline specimen using focused ion beam (FIB). We used the double aberration corrected, monochromated Titan Themis at the Interdisciplinary Centre for Electron Microscopy (CIME) of École Polytechnique Fédérale de Lausanne (EPFL). We acquired spectrum images (see the Supplementary Materials) in the dual EELS mode, which allowed for calibrating the absolute edge energy position and determining chemical shifts in the edge energies associated with changes in valence. We chose to acquire spectra at dispersions of 0.1 eV/channel and dwell time of 50 ms, which provided high energy resolution and produced well-defined *L*-edges above background in a single pixel spectrum but limited the electron beam interactions and radiation damage.

Neutron diffraction experiments

Wide-angle neutron powder diffraction measurements were carried out on a polycrystalline Co_5TeO_8 sample using the high-resolution powder diffractometer (HRPT) of the SINQ instrumental suite at Paul Scherrer Institute (PSI). Data were collected in both medium resolution and high-resolution modes, employing neutrons with a fixed wavelength of 2.45 Å. Each measurement was preceded by a 10-min thermal stabilization period to ensure equilibrium, followed by a 2-h acquisition of high-statistics data.

SANS experiments

SANS experiments, without polarization analysis, were carried out using the SANS-I instrument of Swiss Spallation Neutron Source (SINQ) located at the Paul Scherrer Institute (PSI). About 200 mg of microcrystalline sample was mixed thoroughly with a 1:1 mixture of hydrogen-free FC-77 and FC-75 Fluorinert liquid and enclosed in a vanadium can. The Fluorinert freezes upon cooling to cryogenic temperatures, providing a quasi-strain-free matrix that maintains the random zero-field orientations of the sample grains in finite magnetic field. The can was then installed inside a 6.8-T horizontal field magnet. For all of our experiments, neutrons with wavelength 5 Å with a full width at half maximum (FWHM) spread $\Delta\lambda/\lambda = 10\%$ were used. The incoming neutron beam was collimated by a distance of 8 m before the sample, whereas the scattered neutrons were collected by a 2-dimensional ^{3}He multidetector placed 3.5 m behind the sample.

Uniaxial polarization analysis was performed using the D33 SANS instrument at the Institut Laue-Langevin (ILL), Grenoble. The polycrystalline Co_5TeO_8 sample was embedded in hydrogen-free glue and encapsulated within a vanadium can. Measurements utilized longitudinal polarization geometry with the incident neutron beam collinear to the applied magnetic field. A weak longitudinal magnetic field of 50 mT was applied to the sample, while a 10-mT guide field maintained the neutron spin quantization axis parallel to the incident beam. Scattered neutrons were analyzed using a spin-polarized ^{3}He cell with maximum polarization of 98.6%. Four neutron spin states ($\downarrow\downarrow$, $\uparrow\downarrow$, $\uparrow\uparrow$, and $\downarrow\uparrow$) were systematically measured as a function of temperature during cooling. Neutron beam depolarization was monitored at 2-h intervals in the paramagnetic regime ($T = 65$ K). Data analysis was conducted using GRA$_{SANS}$P software [61].

Cluster-based quantum chemistry calculations

We performed many-body wavefunction calculations on electrostatically embedded finite-size cluster models extracted from the experimental crystal structure. The crystallographic unit cell contains 2 distinct Co^{2+} sites: Co1 atoms in distorted octahedral coordination and Co2 atoms in tetrahedral coordination with oxygen ligands, as shown in Fig. 1A. Our computational models feature a central cluster containing 1 or 2 coordination polyhedra, with the active Co^{2+} centers treated using multireference wavefunctions. Adjacent Co polyhedra representing nearest-neighbor environments were included at the Hartree–Fock level to account for local charge distribution effects. Long-range electrostatic interactions were incorporated through an array of point charges fitted to reproduce the crystalline Madelung potential [62]. Electron correlation effects in the central clusters were described using complete-active-space self-consistent-field (CASSCF) and subsequent multi-reference configuration interaction (MRCI) calculations. The MRCI treatment incorporated single and double excitations from the Co^{2+} 3*d* valence orbitals and the bridging oxygen 2*p* orbitals. Co^{2+} oxidation states were confirmed through EELS measurements (see Section S2), providing the electronic configuration basis for all quantum chemical calculations. The multiplet structure obtained then entered into spin-orbit calculations to obtain spin-orbit coupled eigenstates and wavefunctions [63].

The generalized spin Hamiltonian considered to determine the local magnetic interactions in Co_5TeO_8 can be expressed as

$$\mathcal{H} = \mathcal{H}^{\mathrm{I}} + \mathcal{H}^{\mathrm{II}}, \tag{2}$$

where $\mathcal{H}^{\mathrm{I}}$ denotes the coupling between the *i*th and *j*th nearest-neighbor sites bearing spin S_i and S_j, respectively, while $\mathcal{H}^{\mathrm{II}}$ contains the contribution of the interactions within sites of spin S_i. The intersite contribution, $\mathcal{H}^{\mathrm{I}}$, reads as

$$\mathcal{H}^{\mathrm{I}} = \sum_{\langle ij\rangle=1,2} \mathcal{J}_{ij}\left(S_i \cdot S_j\right) + \mathcal{K}_{ij}\left(S_i \cdot S_j\right)^2 + \mathcal{D}_{ij} \cdot \left(S_i \times S_j\right) \tag{3}$$

where $\mathcal{J}_{ij}$ and $\mathcal{K}_{ij}$ are the bilinear and biquadratic isotropic exchange couplings, respectively, and $\mathcal{D}_{ij}$ is the antisymmetric DMI vector (11, 12). The intra-site contribution $\mathcal{H}^{\mathrm{II}}$ takes the following form:

$$\mathcal{H}^{\mathrm{II}} = \sum_i \mathcal{A}_i \left(S_i \cdot \hat{\mathrm{e}}_i\right)^2 \tag{4}$$

Here, $\mathcal{A}_i$ is the SIA. Further details about our quantum chemistry calculations can be found in Section S5.

Acknowledgments

P.R.B. and J.S.W. thank C. Pfleiderer, S. Seki, S. Hayami, and O. Utesov for fruitful discussions. We thank C. Cayron, B.

Klemke, M. Bonnaud, and O. Zaharko for their help with EBSD, polarization, D33 SANS, and pulsed magnetic field measurements, respectively.
Funding: P.R.B. acknowledges Swiss National Science Foundation (SNSF) Postdoc.Mobility grant P500PT_217697 and Return CH Postdoc.Mobility grant P5R5-2_239356 for financial support. Furthermore, the following SNSF projects are acknowledged: 200021_188707 (P.R.B., V.U., and J.S.W.), 200020_182536 (P.R.B.), and Sinergia Network "NanoSkyrmionics" grant no. CRSII5_171003 (P.R.B., R.Y., V.U., H.M.R., O.V.Y., A.M., and J.S.W.). We acknowledge beamtime allocations from PSI (20200295, 20200297, 20221263, 20222723, 20230476), ILL (5-41-1226), and HLD-HZDR [member of the European Magnetic Field Laboratory (EMFL)] facilities. This work is based partly on experiments performed at the Swiss Spallation Neutron Source SINQ, Paul Scherrer Institute, Villigen, Switzerland. Computations were performed at the Scientific IT and Application Support Center (SCITAS) of EPFL.
Author contributions: P.R.B. and A.M. grew the micro-crystalline sample. Single-crystal diffraction experiments were performed and analyzed by W.H.B. with extensive guidance from A.M. Magnetometry and specific heat measurements were performed by P.R.B. and I.Ž., whereas M.B. performed the capacitance measurements. EELS measurements were performed by P.R.B. and T.L. Wide-angle neutron diffraction was performed by P.R.B., V.U., V.P., H.M.R., and J.S.W. P.R.B., V.U., H.M.R., and J.S.W. performed the nonpolarized SANS, while polarized SANS experiment was performed by P.R.B., V.U., R.C., and N.-J.S. P.R.B. and Y.S. performed the high-field magnetization experiments. Ab initio many-body wavefunction calculations as well as density functional theory calculations were performed by R.Y., with support from O.V.Y. P.R.B. and J.S.W. wrote the manuscript, with input from R.Y. All authors read and commented on the manuscript. P.R.B., O.V.Y., A.M., and J.S.W. jointly conceived the project.
Competing interests: The authors declare that they have no competing interests.

Data Availability

SANS data obtained on the D33 instrument can be found at DOI: https://dx.doi.org/10.5291/ILL-DATA.5-41-1226. All other data can be found in the Zenodo online repository with unique identifier: https://doi.org/10.5281/zenodo.20631317.

Supplementary Materials

Sections S1 to S5
Figs. S1 to S10
Tables S1 and S2

References

1. Fert A, Reyren N, Cros V. Magnetic skyrmions: Advances in physics and potential applications. *Nat Rev Mater*. 2017;2(7):Article 17031.
2. Matsui A, Nomoto T, Arita R. Skyrmion-size dependence of the topological Hall effect: A real-space calculation. *Phys Rev B*. 2021;104(17):Article 174432.
3. Hamamoto K, Ezawa M, Nagaosa N. Quantized topological Hall effect in skyrmion crystal. *Phys Rev B*. 2015;92(11):Article 115417.
4. Kurumaji T, Nakajima T, Hirschberger M, Kikkawa A, Yamasaki Y, Sagayama H, Nakao H, Taguchi Y, Arima TH, Tokura Y. Skyrmion lattice with a giant topological Hall effect in a frustrated triangular-lattice magnet. *Science*. 2019;365(6456):914–918.
5. Ghimire NJ, Dally RL, Poudel L, Jones DC, Michel D, Magar NT, Bleuel M, MA MG, Jiang JS, Mitchell JF, et al. Competing magnetic phases and fluctuation-driven scalar spin chirality in the kagome metal YMn_6Sn_6. *Sci Adv*. 2020;6(51):Article eabe2680.
6. Baral PR, Ukleev V, Živković I, Lee Y, Orlandi F, Manuel P, Skourski Y, Keller L, Stunault A, Rodríguez-Velamazán JA, et al. Fluctuation-driven topological Hall effect in room-temperature itinerant helimagnet Fe_3Ga_4. *Nat Commun*. 2025;16(1):3898.
7. Tokura Y, Seki S. Multiferroics with spiral spin orders. *Adv Mater*. 2010;22(14):1554–1565.
8. Tokura Y, Seki S, Nagaosa N. Multiferroics of spin origin. *Rep Prog Phys*. 2014;77(7):Article 076501.
9. Nagaosa N, Tokura Y. Topological properties and dynamics of magnetic skyrmions. *Nat Nanotechnol*. 2013;8(12):899–911.
10. Tokura Y, Kanazawa N. Magnetic skyrmion materials. *Chem Rev*. 2020;121(5):2857–2897.
11. Dzyaloshinsky I. A thermodynamic theory of "weak" ferromagnetism of antiferromagnetics. *J Phys Chem Solids*. 1958;4(4):241–255.
12. Moriya T. Anisotropic superexchange interaction and weak ferromagnetism. *Phys Rev*. 1960;120(1):91.
13. Bak P, Jensen MH. Theory of helical magnetic structures and phase transitions in MnSi and FeGe. *J Phys C Solid State Phys*. 1980;13(31):L881.
14. Richter J, Darradi R, Schulenburg J, Farnell DJ, Rosner H. Frustrated spin-1/2 J1-J2 Heisenberg ferromagnet on the square lattice studied via exact diagonalization and coupled-cluster method. *Phys Rev B*. 2010;81(17):Article 174429.
15. Okubo T, Chung S, Kawamura H. Multiple-*q* states and the skyrmion lattice of the triangular-lattice Heisenberg antiferromagnet under magnetic fields. *Phys Rev Lett*. 2012;108(1):Article 017206.
16. Bouaziz J, Mendive-Tapia E, Blügel S, Staunton JB. Fermi-surface origin of skyrmion lattices in centrosymmetric rare-earth intermetallics. *Phys Rev Lett*. 2022;128(15):Article 157206.
17. Nomoto T, Koretsune T, Arita R. Formation mechanism of the helical *Q* structure in Gd-based skyrmion materials. *Phys Rev Lett*. 2020;125:Article 117204.
18. Hayami S, Ozawa R, Motome Y. Effective bilinear-biquadratic model for noncoplanar ordering in itinerant magnets. *Phys Rev B*. 2017;95(22):Article 224424.
19. Batista CD, Lin S-Z, Hayami S, Kamiya Y. Frustration and chiral orderings in correlated electron systems. *Rep Prog Phys*. 2016;79(8):Article 084504.
20. Hayami S, Lin S-Z, Batista CD. Bubble and skyrmion crystals in frustrated magnets with easy-axis anisotropy. *Phys Rev B*. 2016;93(18):Article 184413.
21. Hayami S, Motome Y. Noncoplanar multiple-*Q* spin textures by itinerant frustration: Effects of single-ion anisotropy and bond-dependent anisotropy. *Phys Rev B*. 2021;103(5):Article 054422.
22. Lin S-Z, Saxena A, Batista CD. Skyrmion fractionalization and merons in chiral magnets with easy-plane anisotropy. *Phys Rev B*. 2015;91(22):Article 224407.

23. Leonov A, Mostovoy M. Multiply periodic states and isolated skyrmions in an anisotropic frustrated magnet. *Nat Commun*. 2015;6(1):8275.
24. Rinaldi S, Pareti L. A model for a two sublattice system with high competing single ion anisotropies. *J Appl Phys*. 1979;50(B11):7719–7721.
25. Podchezertsev S, Barrier N, Pautrat A, Suard E, Retuerto M, Alonso JA, Fernandez-Diaz MT, Rodriguez-Carvajal J. Influence of polymorphism on the magnetic properties of Co_5TeO_8 spinel. *Inorg Chem*. 2021;60(18):13990–14001.
26. Comin R, Levy G, Ludbrook B, Zhu ZH, Veenstra CN, Rosen JA, Singh Y, Gegenwart P, Stricker D, Hancock JN, et al. Na_2IrO_3 as a novel relativistic Mott insulator with a 340-meV gap. *Phys Rev Lett*. 2012;109(26):Article 266406.
27. Ukleev V, Karube K, Derlet PM, Wang CN, Luetkens H, Morikawa D, Kikkawa A, Mangin-Thro L, Wildes AR, Yamasaki Y, et al. Frustration-driven magnetic fluctuations as the origin of the low-temperature skyrmion phase in $Co_7Zn_7Mn_6$. *npj Quantum Mater*. 2021;6(1):Article 40.
28. Živković I, White JS, Rønnow HM, Prša K, Berger H. Critical scaling in the cubic helimagnet Cu_2OSeO_3. *Phys Rev B*. 2014;89(6):Article 060401.
29. Janoschek M, Garst M, Bauer A, Krautscheid P, Georgii R, Boeni P, Pfleiderer C. Fluctuation-induced first-order phase transition in Dzyaloshinskii-Moriya helimagnets. *Phys Rev B*. 2013;87(13):Article 134407.
30. Kindervater J, Stasinopoulos I, Bauer A, Haslbeck FX, Rucker F, Chacon A, Mühlbauer S, Franz C, Garst M, Grundler D, et al. Weak crystallization of fluctuating skyrmion textures in MnSi. *Phys Rev X*. 2019;9(4):Article 041059.
31. Janson O, Rousochatzakis I, Tsirlin AA, Belesi M, Leonov AA, Rößler UK, Van Den Brink J, Rosner H. The quantum nature of skyrmions and half-skyrmions in Cu_2OSeO_3. *Nat Commun*. 2014;5(1):5376.
32. Kurumaji T, Nakajima T, Feoktystov A, Babcock E, Salhi Z, Ukleev V, Arima TH, Kakurai K, Tokura Y. Direct observation of cycloidal spin modulation and field-induced transition in Néel-type skyrmion-hosting $VOSe_2O_5$. *J Phys Soc Jpn*. 2021;90(2):Article 024705.
33. Takagi R, Matsuyama N, Ukleev V, Yu L, White JS, Francoual S, Mardegan JR, Hayami S, Saito H, Kaneko K, et al. Square and rhombic lattices of magnetic skyrmions in a centrosymmetric binary compound. *Nat Commun*. 2022;13(1):1472.
34. Adams T, Mühlbauer S, Pfleiderer C, Jonietz F, Bauer A, Neubauer A, Georgii R, Böni P, Keiderling U, Everschor K, et al. Long-range crystalline nature of the skyrmion lattice in MnSi. *Phys Rev Lett*. 2011;107(21):Article 217206.
35. Adams T, Chacon A, Wagner M, Bauer A, Brandl G, Pedersen B, Berger H, Lemmens P, Pfleiderer C. Long-wavelength helimagnetic order and skyrmion lattice phase in Cu_2OSeO_3. *Phys Rev Lett*. 2012;108(23):Article 237204.
36. Seki S, Yu XZ, Ishiwata S, Tokura Y. Observation of skyrmions in a multiferroic material. *Science*. 2012;336(6078):198–201.
37. de PR Moreira I, Illas F, Calzado CJ, Sanz JF, Malrieu JP, Amor NB, Maynau D. Local character of magnetic coupling in ionic solids. *Phys Rev B*. 1999;59(10):R6593.
38. Bogdanov NA, van den Brink J, Hozoi L. Ab initio computation of *d-d* excitation energies in low-dimensional Ti and V oxychlorides. *Phys Rev B*. 2011;84(23):Article 235146.
39. Katukuri VM, Stoll H, van den Brink J, Hozoi L. Ab initio determination of excitation energies and magnetic couplings in correlated quasi-two-dimensional iridates. *Phys Rev B*. 2012;85(22):Article 220402.
40. Bogdanov NA, Maurice R, Rousochatzakis I, van den Brink J, Hozoi L. Magnetic state of pyrochlore $Cd_2Os_2O_7$ emerging from strong competition of ligand distortions and longer-range crystalline anisotropy. *Phys Rev Lett*. 2013;110(12):Article 127206.
41. de PR Moreira I, Illas F. A unified view of the theoretical description of magnetic coupling in molecular chemistry and solid state physics. *Phys Chem Chem Phys*. 2006;8(14): 1645–1659.
42. Malrieu JP, Caballol R, Calzado CJ, De Graaf C, Guihery N. Magnetic interactions in molecules and highly correlated materials: Physical content, analytical derivation, and rigorous extraction of magnetic Hamiltonians. *Chem Rev*. 2014;114(1):429–492.
43. Gransbury GK, Boulon ME, Mole RA, Gable RW, Moubaraki B, Murray KS, Sorace L, Soncini A, Boskovic C. Single-ion anisotropy and exchange coupling in cobalt (II)-radical complexes: Insights from magnetic and ab initio studies. *Chem Sci*. 2019;10(38):8855–8871.
44. Tripathi S, Vaidya S, Ahmed N, Klahn EA, Cao H, Spillecke L, Koo C, Spachmann S, Klingeler R, Rajaraman G, et al. Structure-property correlation in stabilizing axial magnetic anisotropy in octahedral Co (II) complexes. *Cell Rep Phys Sci*. 2021;2(4):Article 100404.
45. Lee J, Ma J, Hahn SE, Cao HB, Lee M, Hong T, Lee HJ, Yeom MS, Okamoto S, Zhou HD, et al. Magnetic frustration driven by itinerancy in spinel CoV_2O_4. *Sci Rep*. 2017;7(1):17129.
46. Kismarahardja A, Brooks JS, Kiswandhi A, Matsubayashi K, Yamanaka R, Uwatoko Y, Whalen J, Siegrist T, Zhou HD. $Co[V_2]O_4$: A spinel approaching the itinerant electron limit. *Phys Rev Lett*. 2011;106(5):Article 056602.
47. Katsufuji T, Ikeda H, Ashizawa M, Oike M, Kajita T. Nonlinear behavior in the electrical resistance of strongly correlated insulators. *J Phys Soc Jpn*. 2020;89(4):Article 044702.
48. Shanavas KV, Satpathy S. Electronic structure and the origin of the Dzyaloshinskii-Moriya interaction in MnSi. *Phys Rev B*. 2016;93(19):Article 195101.
49. Heid C, Weitzel H, Burlet P, Bonnet M, Gonschorek W, Vogt T, Norwig J, Fuess H. Magnetic phase diagram of $CoNb_2O_6$: A neutron diffraction study. *J Magn Magn Mater*. 1995;151(1–2):123–131.
50. Baral PR, Utesov OI, Luo C, Radu F, Magrez A, White JS, Ukleev V. Direct observation of exchange anisotropy in the helimagnetic insulator Cu_2OSeO_3. *Phys Rev Res*. 2023;5(3):L032019.
51. Tokunaga Y, Yu XZ, White JS, Rønnow HM, Morikawa D, Taguchi Y, Tokura Y. A new class of chiral materials hosting magnetic skyrmions beyond room temperature. *Nat Commun*. 2015;6(1):7638.
52. Gupta S, Sharma A, Das D, Tulapurkar AA, Muralidharan B. Ultrahigh frequency and multichannel output skyrmion-based nano-oscillator. *IEEE Trans Electron Devices*. 2025:2618–2624.
53. Lee O, Wei T, Stenning KD, Gartside JC, Prestwood D, Seki S, Aqeel A, Karube K, Kanazawa N, Taguchi Y, et al. Task-adaptive physical reservoir computing. *Nat Mater*. 2024;23(1):79–87.
54. Mostovoy M. Multiferroics: Different routes to magnetoelectric coupling. *npj Spintron*. 2024;2(1):18.
55. Che P, Ciola R, Garst M, Kravchuk V, Baral PR, Magrez A, Berger H, Schönenberger T, Rønnow HM, Grundler D.

Short-wave magnons with multipole spin precession detected in the topological bands of a skyrmion lattice. *Commun Mater*. 2025;6(1):139.
56. Ding JK, Zhang EZ, Wang WO, Cookmeyer T, Moritz B, Kim YB, Devereaux TP. Intrinsic thermal Hall effect in Mott insulators. *Phys Rev Lett*. 2025;134(25):Article 256501.
57. Stoliar P, Cario L, Janod E, Corraze B, Guillot-Deudon C, Salmon-Bourmand S, Guiot V, Tranchant J, Rozenberg M. Universal electric-field-driven resistive transition in narrow-gap Mott insulators. *Adv Mater*. 2013;25(23):3222–3226.
58. Kresse G, Furthmüller J. Efficient iterative schemes for ab initio total-energy calculations using a plane-wave basis set. *Phys Rev B*. 1996;54:11169–11186.
59. Blöchl PE. Projector augmented-wave method. *Phys Rev B*. 1994;50:17953.
60. Dudarev SL, Botton GA, Savrasov SY, Humphreys CJ, Sutton AP. Electron-energy-loss spectra and the structural stability of nickel oxide: An LSDA+*U* study. *Phys Rev B*. 1998;57(3):1505.
61. Dewhurst CD. Graphical reduction and analysis small-angle neutron scattering program: GRASP. *J Appl Crystallogr*. 2023;56(5):1595–1609.
62. Klintenberg M, Derenzo SE, Weber MJ. Accurate crystal fields for embedded cluster calculations. *Comput Phys Commun*. 2000;131(1–2):120–128.
63. Helgaker T, Jorgensen P, Olsen J. *Molecular electronic-structure theory*. New York (NY): John Wiley & Sons; 2014.
64. Singh D, Fujishiro Y, Hayami S, Moody SH, Nomoto T, Baral PR, Ukleev V, Cubitt R, Steinke NJ, Gawryluk DJ, et al. Transition between distinct hybrid skyrmion textures through their hexagonal-to-square crystal transformation in a polar magnet. *Nat Commun*. 2023;14(1):8050.
65. Kaneko K, Frontzek MD, Matsuda M, Nakao A, Munakata K, Ohhara T, Kakihana M, Haga Y, Hedo M, Nakama T, et al. Unique helical magnetic order and field-induced phase in trillium lattice antiferromagnet EuPtSi. *J Phys Soc Jpn*. 2019;88(1):Article 013702.
66. Kanazawa N, Kim JH, Inosov DS, White JS, Egetenmeyer N, Gavilano JL, Ishiwata S, Onose Y, Arima TH, Keimer B, et al. Possible skyrmion-lattice ground state in the *B*20 chiral-lattice magnet MnGe as seen via small-angle neutron scattering. *Phys Rev B*. 2012;86(13):Article 134425.
67. Matsumura T, Kita Y, Kubo K, Yoshikawa Y, Michimura S, Inami T, Kousaka Y, Inoue K, Ohara S. Chiral soliton lattice formation in monoaxial helimagnet $Yb(Ni_{1-x}Cu_x)_3Al_9$. *J Phys Soc Jpn*. 2017;86(12):Article 124702.
68. Marty K, Simonet V, Ressouche E, Ballou R, Lejay P, Bordet P, Bordallo HN, Hardy V, Hezaim J, Maignan A, et al. Magnetic properties of the Fe langasite $Ba_3NbFe_3Si_2O_{14}$: A chiral spin liquid candidate. *Phys Rev Lett*. 2008;101:Article 247201.
69. Puphal P, Pomjakushin V, Kanazawa N, Ukleev V, Gawryluk DJ, Ma J, Naamneh M, Plumb NC, Keller L, Cubitt R, et al. Topological magnetic phase in the candidate Weyl semimetal CeAlGe. *Phys Rev Lett*. 2020;124(1): Article 017202.
70. Takagi R, White JS, Hayami S, Arita R, Honecker D, Rønnow HM, Tokura Y, Seki S. Multiple-*q* noncollinear magnetism in an itinerant hexagonal magnet. *Sci Adv*. 2018;4(11):Article eaau3402.
71. Makino K, Okuyama D, Avdeev M, Sato TJ. Incommensurate magnetic structure in the cubic noncentrosymmetric ternary compound $Pr_5Ru_3Al_2$. *J Phys Soc Jpn*. 2016;85(7): Article 073705.
72. Araki Y, Sato T, Fujima Y, Abe N, Tokunaga M, Kimura S, Morikawa D, Ukleev V, Yamasaki Y, Tabata C, et al. Metamagnetic transitions and magnetoelectric responses in the chiral polar helimagnet Ni_2InSbO_6. *Phys Rev B*. 2020;102(5):Article 054409.
73. Muhlbauer S, Binz B, Jonietz F, Pfleiderer C, Rosch A, Neubauer A, Georgii R, Boni P. Skyrmion lattice in a chiral magnet. *Science*. 2009;323(5916):915–919.
74. Mühlbauer S, Gvasaliya S, Ressouche E, Pomjakushina E, Zheludev A. Phase diagram of the Dzyaloshinskii-Moriya helimagnet $Ba_2CuGe_2O_7$ in canted magnetic fields. *Phys Rev B*. 2012;86(2):Article 024417.
75. Kézsmárki I, Bordács S, Milde P, Neuber E, Eng LM, White JS, Rønnow HM, Dewhurst CD, Mochizuki M, Yanai K, et al. Néel-type skyrmion lattice with confined orientation in the polar magnetic semiconductor GaV_4S_8. *Nat Mater*. 2015;14(11):1116–1122.
76. Kousaka Y, Ogura T, Zhang J, Miao P, Lee S, Torii S, Kamiyama T, Campo J, Inoue K, Akimitsu J. Long periodic helimagnetic ordering in CrM_3S_6 (*M*= Nb and ta). *J Phys Conf Ser*. 2016;746:Article 012061.
77. Grigoriev S, Chernyshov D, Dyadkin VA, Dmitriev V, Maleyev SV, Moskvin EV, Menzel D, Schoenes J, Eckerlebe H. Crystal handedness and spin helix chirality in $Fe_{1-x}Co_xSi$. *Phys Rev Lett*. 2009;102(3):Article 037204.
78. Togawa Y, Koyama T, Takayanagi K, Mori S, Kousaka Y, Akimitsu J, Nishihara S, Inoue K, Ovchinnikov AS, Kishine JI. Chiral magnetic soliton lattice on a chiral helimagnet. *Phys Rev Lett*. 2012;108(10):Article 107202.
79. Sosnowska I, Neumaier TP, Steichele E. Spiral magnetic ordering in bismuth ferrite. *J Phys C Solid State Phys*. 1982;15(23):4835–4846.
80. Yu X, Kanazawa N, Onose Y, Kimoto K, Zhang WZ, Ishiwata S, Matsui Y, Tokura Y. Near room-temperature formation of a skyrmion crystal in thin-films of the helimagnet FeGe. *Nat Mater*. 2011;10(2):106–109.
81. Li W, Jin C, Che R, Wei W, Lin L, Zhang L, Du H, Tian M, Zang J. Emergence of skyrmions from rich parent phases in the molybdenum nitrides. *Phys Rev B*. 2016;93(6):Article 060409.
82. Janoschek M, Fischer P, Schefer J, Roessli B, Pomjakushin V, Meven M, Petricek V, Petrakovskii G, Bezmaternikh L. Single magnetic chirality in the magnetoelectric $NdFe_3(^{11}BO_3)_4$. *Phys Rev B*. 2010;81(9):Article 094429.
83. Kurumaji T, Nakajima T, Ukleev V, Feoktystov A, Arima TH, Kakurai K, Tokura Y. Néel-type skyrmion lattice in the tetragonal polar magnet $VOSe_2O_5$. *Phys Rev Lett*. 2017;119(23):Article 237201.
84. Nayak AK, Kumar V, Ma T, Werner P, Pippel E, Sahoo R, Damay F, Rößler UK, Felser C, Parkin SS. Magnetic antiskyrmions above room temperature in tetragonal Heusler materials. *Nature*. 2017;548(7669):561–566.
85. Karube K, Peng L, Masell J, Yu X, Kagawa F, Tokura Y, Taguchi Y. Room-temperature antiskyrmions and sawtooth surface textures in a non-centrosymmetric magnet with S_4 symmetry. *Nat Mater*. 2021;20(3):335–340.